

Effect of nuclear density profile on the global properties in O+O collisions at the Large Hadron Collider using a multi-phase transport model

Debadatta Behera¹, Neelkamal Mallick¹, Sushanta Tripathy³,
Suraj Prasad¹, Aditya Nath Mishra⁴, and Raghunath Sahoo^{1,2*}

¹*Department of Physics, Indian Institute of Technology Indore, Simrol, Indore 453552, India*

²*CERN, CH 1211, Geneva 23, Switzerland*

³*INFN - sezione di Bologna, via Irmerio 46, 40126 Bologna BO, Italy and*

⁴*Wigner Research Center for Physics, H-1121 Budapest, Hungary*

(Dated: October 11, 2021)

Oxygen (¹⁶O) ions are planned to be injected at the Large Hadron Collider (LHC) in its next runs and a day of physics run is anticipated for O+O collisions at $\sqrt{s_{NN}} = 7$ TeV. As the system size of O+O collisions is in between those produced in pp and p+Pb collisions, the study of global properties in O+O collisions may provide a deeper insight into the heavy-ion-like behavior observed in small collision systems and its similarities/differences with larger system like Pb+Pb collisions. In the present work, we report the predictions for global properties in O+O collisions at $\sqrt{s_{NN}} = 7$ TeV using a multi-phase transport model (AMPT). We report the mid-rapidity charged particle multiplicity, transverse mass, Bjorken energy density, pseudorapidity distributions, speed of sound, transverse momentum (p_T) spectra, the kinetic freeze-out parameters and p_T -differential particle ratio as a function of collision centrality. Further, we have studied the transverse momentum dependent elliptic flow of charged particles. The results are shown for Woods-Saxon and harmonic oscillator nuclear density profiles incorporated inside oxygen nucleus. With the change of the density profile with harmonic oscillator from Woods-Saxon, a modification of average charged-particle multiplicity at most central collisions is seen. Bjorken energy density show a significant increase in most central collisions for harmonic oscillator density profile while other global properties show less dependence on the density profiles considered in this work.

PACS numbers:

I. INTRODUCTION

In order to understand the properties of hot and dense medium, often referred as Quark Gluon Plasma (QGP), formed in ultra-relativistic heavy-ion collisions at the Large Hadron Collider (LHC) and Relativistic Heavy Ion collider (RHIC), several measurements in different collision systems at different center-of-mass energies are performed. Historically in these collider experiments, heavy-ion collisions such as Pb+Pb and Au+Au collisions are the primary focus in the study of QGP while the small collision systems such as proton-proton (pp) collisions act as a baseline. However, recent results from LHC experiments [1, 2] show QGP-like properties in high-multiplicity pp collisions, which raises concerns in the heavy-ion physics community whether pp collisions can act as a baseline and in addition, if QGP-droplets are produced in the collisions of small systems at the LHC energies. This ambiguity has a serious consequence on the results reported for heavy-ion collisions. Thus, a closer look at the small collision systems is a call of time.

In the upcoming run at the LHC, a brief oxygen-oxygen (O+O) collisions is anticipated [3], which has final state multiplicity overlap with pp and p+Pb collisions. Recently, several theoretical studies on O+O collisions have been performed [4–7]. A detailed study on system formed

in O+O collisions may give a deeper insight into understanding the QGP-like properties in small collision systems. As ¹⁶O is doubly magic, it is assumed to be stable against decay and has very compact structure [8]. Also, α -clustered structure [9] is proposed to affect oxygen nuclei, where the mean field effect is not strong enough to break the cluster structure. The α -clustering in a nucleus appears when two protons and two neutrons cluster together. A signature of α -clustering is seen in recent simulation studies for collisions involving oxygen nuclei [9]. However, solid experimental evidences are not yet in place in support of the exotic tetrahedral α -clustering structure of ¹⁶O nucleus, which was originally proposed by G. Gamow [10] and then by J.A. Wheeler [11]. The nuclear structure, though conventionally probed in low-energy nuclear experiments, can also be probed in ultra-relativistic heavy-ion collisions through the final state observables, which are sensitive to the initial nuclear geometry. In particular, probing the α -clustering structure in relativistic collisions of light nuclei are being conjectured and studied extensively by Broniowski *et al.* [12–14]. In a basic nuclear shell model calculation [15], the potential inside nucleus is assumed to be simple harmonic oscillator potential and then a spin-orbit interaction term is added. From this calculation the magic numbers are obtained and the nucleus with these magic number of nucleons are expected to be tightly bound and highly stable. As the number of protons and neutrons in oxygen match the magic number individually, the oxygen nucleus is doubly magic and it is expected to be highly compact. To

*Corresponding author: *Raghunath.Sahoo@cern.ch*

get a deeper insight on the impact of nuclear structure inside the oxygen nucleus, we have incorporated simple harmonic oscillator potential and more realistic Woods-Saxon potential in oxygen nucleus using a multi-phase transport model (AMPT) [16]. Oxygen has also got an isotope (^{24}O), which is doubly magic with eight protons and sixteen neutrons but unstable in nature. Readers can refer to Ref. [17] for the details of the nuclear structure of ^{24}O , as an outlook.

Global observables like charged-particle multiplicities, transverse energy, particle spectra and pseudorapidity distributions provide insight about the possible formation of QGP in a system. It is proposed that the equation of state of hot hadronic matter can be probed via the correlation of mean transverse momentum and particle multiplicity [18]. Charged-particle multiplicity provides information about the soft processes in the collision, while the mean transverse mass and momentum gives insight to the hard processes. In recent results from the LHC [1], it has been shown that the QGP-like properties seen in high-multiplicity pp collisions are driven by the final state multiplicity in an event. Thus, it would be interesting to confront initial and final state effects in O+O collisions as it has multiplicity overlap with high-multiplicity pp collisions. The initial energy density can be estimated by using Bjorken hydrodynamic model [19], where one uses the transverse energy or charged particle multiplicity density in rapidity and mean transverse mass for each collision centrality. To explore, the final state effects, a study on particle spectra, kinetic freeze out parameters and particle ratios can be studied. In this work, the global properties [20] such as Bjorken energy density, speed of sound, particle ratios and kinetic freezeout parameters are studied for O+O collisions at $\sqrt{s_{\text{NN}}} = 7$ TeV using AMPT for both harmonic oscillator and Woods-Saxon nuclear density profile incorporated in oxygen nucleus, in order to explore the effect of nuclear density profile of the final state observables. In addition, these findings, when confronted to the available experimental data in due course would reveal the nuclear density profile of Oxygen nucleus from the observations of ultra-relativistic nuclear collisions.

The paper is organised as follows. We begin with a brief introduction about O+O collisions in Section I. In Section II, the detailed event generation methodology with AMPT along with different types of nuclear density profile are discussed. Section III discusses about the results. Finally, the results are summarized in Section VI with possible outlook.

II. EVENT GENERATION AND ANALYSIS METHODOLOGY

In this section, we begin with a brief introduction on AMPT model and then discuss about the charge density profile of oxygen.

A. A Multi-Phase Transport (AMPT) Model

AMPT model primarily consists of four components [16]: 1. initialization of the collisions using HIJING [21], where the differential cross-section of the produced mini-jets in pp collisions is calculated and converted to heavy-ion collisions with inbuilt Glauber model, 2. the produced partons are propagated into parton transport part via Zhang's Parton Cascade (ZPC) model [22], 3. hadronization mechanism: in AMPT string melting version, the transported partons are hadronized using spatial coalescence mechanism [23, 24], 4. hadron transport: the produced hadrons undergo final evolution in relativistic transport mechanism [25, 26] via baryon-baryon, meson-baryon and meson-meson interactions. Although there is also a default version available in AMPT, we have used string melting mode of AMPT (AMPT version 2.26t9b) in the current work due to the fact that the particle flow and spectra at the intermediate- p_{T} regions are well explained by quark coalescence mechanism available in the string melting version for hadronization [27–29]. We have used the similar AMPT settings in the current work as reported in Ref. [30] unless specified explicitly. As there is no experimental data available for O+O collisions, we have compared the charged particle p_{T} -spectra from minimum bias p+Pb collisions at $\sqrt{s_{\text{NN}}} = 5.02$ TeV in midrapidity with the predictions from AMPT fixing the partonic scattering cross section, $\sigma_{\text{gg}} = 3$ mb [4], which can be seen in the Appendix section of the paper.

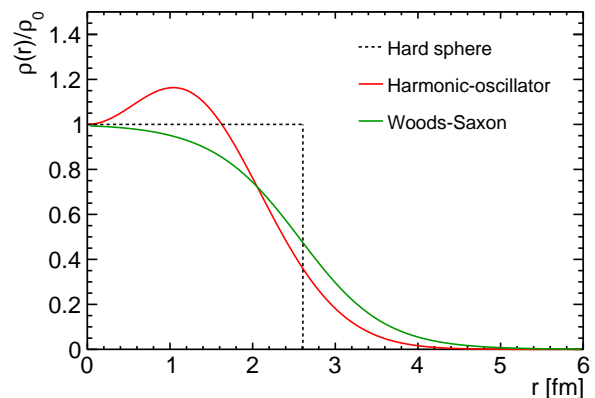


FIG. 1: (Color Online) Nuclear density profile for oxygen nucleus. Shown are the hard sphere, harmonic oscillator and Woods-Saxon density profiles.

The collision centrality, the number of participants (N_{part}) and the number of binary collisions (N_{coll}) in heavy-ion collisions cannot be determined directly from experiments, instead it is obtained via the impact parameter determination in the Glauber model [31–33]. The Glauber model considers a nucleus-nucleus collision as a superposition of several independent nucleon-nucleon collisions and the estimations are dependent on the nuclear density profile. In this work, we have modified the inbuilt

TABLE I: The impact parameter, average number of nucleon participants and average number of nucleon-nucleon binary collisions for different density profiles and in different centrality classes for O+O collisions at $\sqrt{s_{NN}} = 7$ TeV. Centrality selection is done through geometrical slicing, *i.e.* from the impact parameter.

Centrality(%)	Woods-Saxon				harmonic oscillator			
	b_{\min} (fm)	b_{\max} (fm)	$\langle N_{\text{part}} \rangle$	$\langle N_{\text{coll}} \rangle$	b_{\min} (fm)	b_{\max} (fm)	$\langle N_{\text{part}} \rangle$	$\langle N_{\text{coll}} \rangle$
0–5	0	1.47	28.00 ± 2.06	48.33 ± 9.43	0	1.28	29.48 ± 1.61	63.83 ± 11.32
5–10	1.47	2.08	25.22 ± 2.27	39.96 ± 7.98	1.28	1.83	27.06 ± 2.00	52.64 ± 9.17
10–20	2.08	2.94	21.25 ± 2.81	30.17 ± 7.34	1.83	2.58	23.20 ± 2.68	39.31 ± 8.57
20–30	2.94	3.59	16.46 ± 3.01	20.24 ± 5.96	2.58	3.17	18.30 ± 2.94	26.21 ± 6.95
30–40	3.59	4.14	12.55 ± 3.20	13.63 ± 5.07	3.17	3.66	14.12 ± 3.17	17.55 ± 6.00
40–50	4.14	4.63	9.39 ± 3.15	9.13 ± 4.22	3.66	4.10	10.46 ± 3.21	11.33 ± 4.98
50–60	4.63	5.09	7.01 ± 2.86	6.17 ± 3.40	4.10	4.51	7.76 ± 2.99	7.43 ± 3.98
60–70	5.09	5.54	5.32 ± 2.45	4.27 ± 2.65	4.51	4.89	5.76 ± 2.57	4.96 ± 3.07
70–100	5.54	13.46	3.33 ± 1.68	2.28 ± 1.68	4.89	9.86	3.47 ± 1.76	2.47 ± 1.86

Glauber model in AMPT to incorporate harmonic oscillator density profile and compared the results with that of Woods-Saxon nuclear density profile. The values of impact parameter for different centrality classes in O+O collisions are obtained by using the publicly available MC Glauber code (TGlauberMC-3.2) [34–37]. The values of impact parameter, average number of nucleon participants and average number of binary nucleon-nucleon collisions for different density profiles and in different centrality classes are shown in Table I.

B. Woods-Saxon density profile

In high-energy heavy-ion collisions, the standard method employed for nuclear density profile is in terms of three-parameter Fermi (3pF) distributions, which is often referred as Woods-Saxon distribution. The Woods-Saxon distribution is given by,

$$\rho(r) = \frac{\rho_0(1 + w(\frac{r}{r_0})^2)}{1 + \exp(\frac{r-r_0}{a})}. \quad (1)$$

Here, r is the radial distance from the center of the nucleus, r_0 is the mean radius of the nucleus, a is the skin depth/diffusivity of the nucleus and w is the deformation parameter. For oxygen nucleus, r_0 is 2.608 fm, a is 0.513 fm, w is -0.051. ρ_0 is the nuclear density constant at $r = 0$, which is obtained by the overall normalization condition,

$$\int \rho(r)d^3r = 4\pi \int \rho(r)r^2dr = A. \quad (2)$$

Here, A is the mass number of the nucleus *i.e.*, 16 for oxygen nucleus. For a hard sphere configuration in $r < r_0$, $\rho(r) = \rho_0$ and $\rho_0 = 3A/(4\pi R^3)$.

C. Harmonic oscillator density profile

The harmonic oscillator charge density distribution is given by,

$$\rho(r) = \rho_0 \left[1 + \alpha \left(\frac{r}{a} \right)^2 \right] \exp\left(\frac{-r^2}{a^2} \right). \quad (3)$$

Here, a and α are parameters which are taken as 1.544 fm and 1.833 for oxygen [37], respectively. Similar to the Woods-Saxon case, ρ_0 is the nuclear density constant at $r = 0$, which should satisfy the normalization condition mentioned in Eq. 2.

Figure 1 shows the comparison of different normalised hard sphere, Woods-Saxon and harmonic oscillator nuclear density profiles of oxygen. A significant rise of the normalised density profile at small r due to harmonic oscillator potential is seen with respect to Woods-Saxon density profile.

III. RESULTS AND DISCUSSIONS

Here, we discuss the predictions for different global properties such as Bjorken energy density, speed of sound, freeze-out parameters as a function of centrality class in different subsections. We have also studied the transverse momentum dependent elliptic flow of charged particles. Here onwards for simplicity, we refer $\pi^+ + \pi^-$, $K^+ + K^-$ and $p + \bar{p}$ as pions, kaons and protons, respectively.

A. Transverse energy and Bjorken Energy Density

In the study of QGP properties in heavy-ion collisions, one of the key variables is the initial energy density produced in such collisions. The initial density can be estimated via the Bjorken boost-invariant hydrodynamics

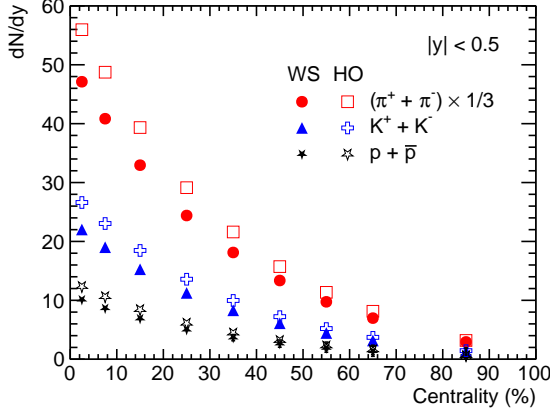


FIG. 2: (Color Online) Integrated yield of pions, kaons and protons at mid-rapidity as a function centrality classes for pions, kaons and protons in O+O collisions at $\sqrt{s_{NN}} = 7$ TeV. The solid markers represent the Woods-Saxon (WS) density profile and open markers represent harmonic oscillator (HO) density profile.

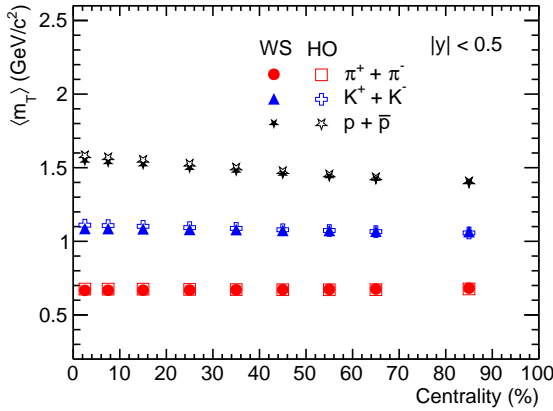


FIG. 3: (Color Online) Mean transverse mass as a function centrality classes for pions, kaons and protons in O+O collisions at $\sqrt{s_{NN}} = 7$ TeV. The solid markers represent the Woods-Saxon (WS) density profile and open markers represent harmonic oscillator (HO) density profile.

model [19], where transverse energy density (E_T) in mid-rapidity gives the quantitative estimation of the initial energy density produced in the interaction. The Bjorken energy density (ϵ_{Bj}) with the assumption of boost invariance is given as,

$$\epsilon_{Bj} = \frac{1}{\tau S_T} \frac{dE_T}{dy}, \quad (4)$$

where, S_T is the transverse overlap area of the two colliding nuclei and dE_T/dy is the transverse energy density at midrapidity at a formation time τ . As Eq. 4 diverges at $\tau \rightarrow 0$, a finite formation time ($\tau = 1$ fm/c) is assumed for the calculation of Bjorken energy density in

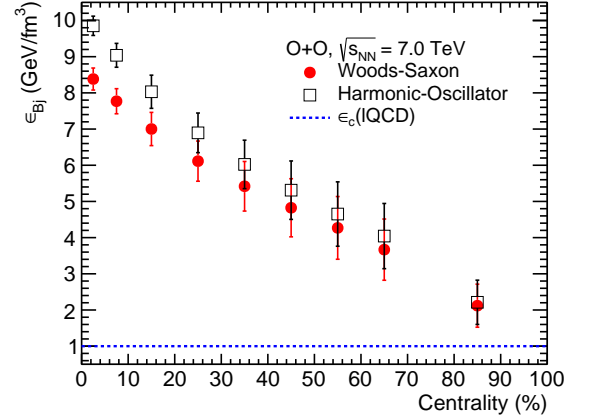


FIG. 4: (Color Online) Bjorken energy density as a function centrality classes for pions, kaons and protons in O+O collisions at $\sqrt{s_{NN}} = 7$ TeV. The solid (open) markers represent the Woods-Saxon (harmonic oscillator) density profile.

this work. E_T is the total transverse energy produced in an event and $S_T = \pi R^2$ is the total transverse overlap area of the colliding nuclei. Replacing, $R = R_0 A^{1/3}$ and $A = N_{part}/2$,

$$S_T = \pi R_0^2 \left(\frac{N_{part}}{2} \right)^{2/3} \quad (5)$$

As most of the transverse energy is carried by the pions, kaons and protons due to their abundance, the total transverse energy (E_T) can be approximated as [38–40],

$$\frac{dE_T}{dy} \approx \frac{3}{2} \times \left(\langle m_T \rangle \frac{dN}{dy} \right)_{\pi^\pm} + 2 \times \left(\langle m_T \rangle \frac{dN}{dy} \right)_{K^\pm, p, \bar{p}}. \quad (6)$$

The multiplicative factor in each term accounts for corresponding neutral particles. $\langle m_T \rangle (= \sqrt{p_T^2 + m^2})$ is the mean transverse momentum and dN/dy is the integrated yield for π^\pm , K^\pm and $p + \bar{p}$ in mid-rapidity region *i.e.* $|y| < 0.5$. Now, Eq. 4 can be written as,

$$\epsilon_{Bj} \approx \frac{1}{\tau \pi R_0^2 \left(\frac{N_{part}}{2} \right)^{2/3}} \left[\frac{3}{2} \times \left(\langle m_T \rangle \frac{dN}{dy} \right)_{\pi^\pm} + 2 \times \left(\langle m_T \rangle \frac{dN}{dy} \right)_{K^\pm, p, \bar{p}} \right] \quad (7)$$

Figures 2 and 3 show the integrated yields and mean transverse momenta for pions, kaons and protons as a function of centrality classes for O+O collisions at $\sqrt{s_{NN}} = 7$ TeV, respectively. The solid markers represent the Woods-Saxon density profile while the open markers represent the results for harmonic oscillator density profile. As expected, the integrated yield of pions are higher compared to kaons and protons as they are most abundant among the identified particles and is understood from a

thermalized Boltzmannian production of secondaries in nuclear collisions. The comparison of Woods-Saxon density profile with harmonic oscillator density profile shows that the soft particle production is higher for harmonic oscillator density profile in central collisions. However, the mean transverse mass remains nearly the same indicating similar spectral shape for both the density profiles. For peripheral collisions, the differences between the density profiles diminishes.

With the input of integrated yields and mean transverse momenta for pions, kaons and protons, the Bjorken energy density is obtained as a function centrality classes using Eq. 7, which is shown in Fig. 4. The solid markers represent the Woods-Saxon density profile while the open markers represent the results for harmonic oscillator density profile. The Bjorken energy density is found to be higher for most central collisions and linearly decreases while going from central to peripheral collisions. As evident in Eq. 7, Bjorken energy density strongly depends on the integrated yield and the difference of integrated yield for different nuclear density profile is reflected in the Bjorken energy density. The oxygen nucleus with harmonic oscillator density profile shows about 15% higher energy density compared to Woods-Saxon density profile. Thus, for central O+O collisions the density profile plays a crucial role in studying the initial-state (Bjorken energy density) and final-state (integrated yields) effects. However, going towards higher impact parameter, *i.e.*, for peripheral collisions the difference is negligible. The nuclear density profile has a clear effect on the initial energy density, which in fact controls the particle production and the subsequent space-time evolution of the fireball, and hence the equation of state (EoS). The values of the initial energy densities for all collision centralities are observed to be higher than the lattice QCD estimated requirement of 1 GeV/fm³ energy density for a deconfinement transition [41]. This hints for observing the signals of QGP in oxygen-oxygen collisions at the LHC energies. We shall further strengthen these arguments in the following sections while discussing on other global observables in heavy-ion collisions.

B. Pseudorapidity distributions and speed of sound

Figure 5 shows pseudorapidity distributions of charged particles in O+O collisions at $\sqrt{s_{NN}} = 7$ TeV for (0-5)% and (70-100)% centrality classes for both Woods-Saxon and harmonic oscillator density profiles. Here, the differences in the charged particle multiplicity in the mid-pseudorapidity due to modification of nuclear density profiles is clearly visible for central collisions while the difference is relatively smaller for peripheral collisions. However, at forward-pseudorapidity, almost no dependence of charged-particle density due to density profiles is seen.

In Landau hydrodynamical model [42], the rapidity distributions are expected to follow a Gaussian distri-

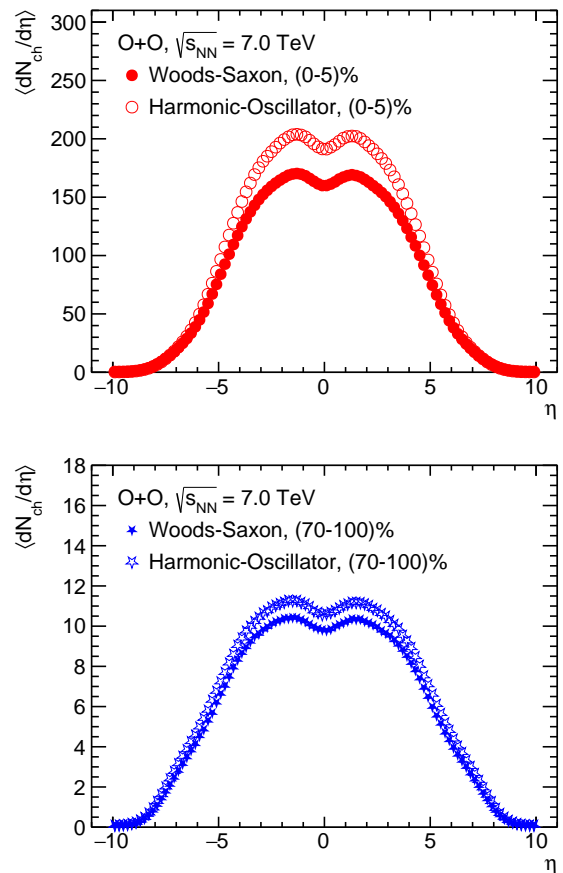


FIG. 5: (Color Online) Pseudorapidity distributions of charged particles in O+O collisions at $\sqrt{s_{NN}} = 7$ TeV for (0-5)% (top) and (70-100)% (bottom) centrality classes. The solid (open) markers represent the Woods-Saxon (harmonic oscillator) density profile.

bution and in this framework, the speed of sound (c_s) is related to the width of the rapidity distribution via the following expression.

$$\sigma_y^2 = \frac{8}{3} \frac{c_s^2}{1 - c_s^2} \ln \left(\frac{\sqrt{s_{NN}}}{2m_p} \right). \quad (8)$$

Here, σ_y is the width of the rapidity distribution and m_p is the mass of proton. The ideal gas limit for the squared speed of sound (c_s^2) is 0.33. However, the presence of the dip structure in pseudorapidity distributions at mid-pseudorapidity makes it difficult to fit via a single Gaussian distribution. Usually in experiments [43, 44], the following double Gaussian distribution is used to fit the pseudorapidity distributions to extrapolate the distributions to the unmeasured regions:

$$A_1 e^{-\frac{\eta^2}{2\sigma_1^2}} - A_2 e^{-\frac{\eta^2}{2\sigma_2^2}}. \quad (9)$$

Here, A_1 and A_2 are the normalization parameters while σ_1 and σ_2 are the widths of each Gaussian distribution.

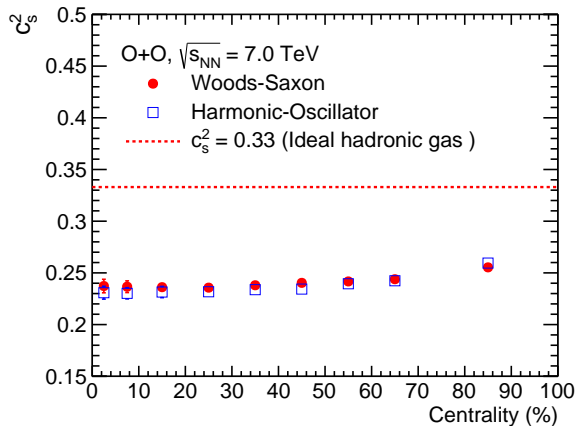


FIG. 6: (Color Online) Squared speed of sound as a function centrality classes for pions, kaons and protons in O+O collisions at $\sqrt{s_{NN}} = 7$ TeV. The solid (open) markers represent the Woods-Saxon (harmonic oscillator) potential.

Thus, using Eq. 9 for the fitting of pseudorapidity distributions, we have obtained σ_1 and σ_2 . The values of σ_1 and σ_2 are found to be similar within uncertainties, which can be seen in Table II. Figure 6 shows the squared speed of sound as a function centrality classes for pions, kaons and protons in O+O collisions at $\sqrt{s_{NN}} = 7$ TeV for both Woods-Saxon and harmonic oscillator density profiles obtained using Eq. 8. Here, σ_1 has been used to obtain the absolute value and the maximum deviation of σ_1 and σ_2 is used as uncertainties for c_s^2 . Considering the uncertainties, c_s^2 is found to be similar as a function of centrality. The negligible dependence of c_s^2 on centrality classes could give an indication that the system produced in O+O collisions is significantly less dense compared Pb+Pb collisions and they are more similar to pp collisions. The ideal gas limit is also shown as a red dotted line in Fig. 6 and the observed values of c_s^2 are found to be around 27% lower than the ideal gas limit.

TABLE II: Double-gaussian width parameters from fitting the pseudorapidity distributions in the range $|\eta| < 3$ using Eq. 9.

Centrality(%)	Woods-Saxon		harmonic oscillator	
	σ_1	σ_2	σ_1	σ_2
0–5	2.35 ± 0.04	2.22 ± 0.04	2.31 ± 0.04	2.20 ± 0.04
5–10	2.34 ± 0.04	2.24 ± 0.04	2.31 ± 0.04	2.24 ± 0.03
10–20	2.34 ± 0.03	2.25 ± 0.03	2.32 ± 0.04	2.21 ± 0.03
20–30	2.34 ± 0.02	2.27 ± 0.03	2.32 ± 0.03	2.24 ± 0.03
30–40	2.35 ± 0.02	2.30 ± 0.02	2.33 ± 0.02	2.27 ± 0.02
40–50	2.36 ± 0.01	2.33 ± 0.01	2.33 ± 0.02	2.29 ± 0.02
50–60	2.37 ± 0.01	2.35 ± 0.01	2.36 ± 0.01	2.33 ± 0.01
60–70	2.38 ± 0.01	2.36 ± 0.01	2.38 ± 0.01	2.35 ± 0.01
70–100	2.48 ± 0.01	2.44 ± 0.01	2.47 ± 0.01	2.46 ± 0.01

C. p_T -spectra and kinetic freeze-out parameters

Figure 7 shows the simultaneous fitting of identified particles' p_T -spectra with Boltzmann-Gibbs blastwave distribution in O+O collisions at $\sqrt{s_{NN}} = 7$ TeV for (0-5)% (top) and (70-100)% (bottom) centrality classes. The left (right) plots show the fitting with Woods-Saxon (Harmonic Oscillator) density profiles in Oxygen nucleus. The fitting ranges for each particle is similar to the range reported by ALICE [45]. The fitting is performed via the χ^2 -minimisation method and the values of χ^2 per degrees of freedom is shown in each of the cases in Fig 7. The expression for invariant yield in the Boltzmann-Gibbs blastwave framework [46] is given as the following:

$$E \frac{d^3 N}{dp^3} = C \int d^3 \sigma_\mu p^\mu \exp\left(-\frac{p^\mu u_\mu}{T}\right). \quad (10)$$

Here C is the normalisation constant. The particle four-momentum is given by,

$$p^\mu = (m_T \cosh y, p_T \cos \phi, p_T \sin \phi, m_T \sinh y), \quad (11)$$

and the four-velocity is given by,

$$u^\mu = \cosh \rho (\cosh \eta, \tanh \rho \cos \phi_r, \tanh \rho \sin \phi_r, \sinh \eta). \quad (12)$$

Finally, the freeze-out surface is parametrised as,

$$d^3 \sigma_\mu = (\cosh \eta, 0, 0, -\sinh \eta) \tau r dr d\eta d\phi_r. \quad (13)$$

here, η is the space-time rapidity. Now, Eq. 10 is expressed as,

$$\left. \frac{d^2 N}{dp_T dy} \right|_{y=0} = C \int_0^{R_0} r dr K_1\left(\frac{m_T \cosh \rho}{T_{th}}\right) I_0\left(\frac{p_T \sinh \rho}{T_{th}}\right). \quad (14)$$

Here, g is the degeneracy factor. $K_1\left(\frac{m_T \cosh \rho}{T_{th}}\right)$ and $I_0\left(\frac{p_T \sinh \rho}{T_{th}}\right)$ are modified Bessel's functions, which are given by,

$$K_1\left(\frac{m_T \cosh \rho}{T}\right) = \int_0^\infty \cosh y \exp\left(-\frac{m_T \cosh y \cosh \rho}{T_{th}}\right) dy,$$

$$I_0\left(\frac{p_T \sinh \rho}{T}\right) = \frac{1}{2\pi} \int_0^{2\pi} \exp\left(\frac{p_T \sinh \rho \cos \phi}{T_{th}}\right) d\phi,$$

where, ρ is given by $\rho = \tanh^{-1} \beta_T$ and $\beta_T (= \beta_s \xi^n)$ [46–49] is the radial flow. Here, ξ is given as (r/R_0) , β_s is the maximum surface velocity and r is the radial distance. R_0 is the maximum radius of the source at freeze-out. In this model, the particles closer to the center of the

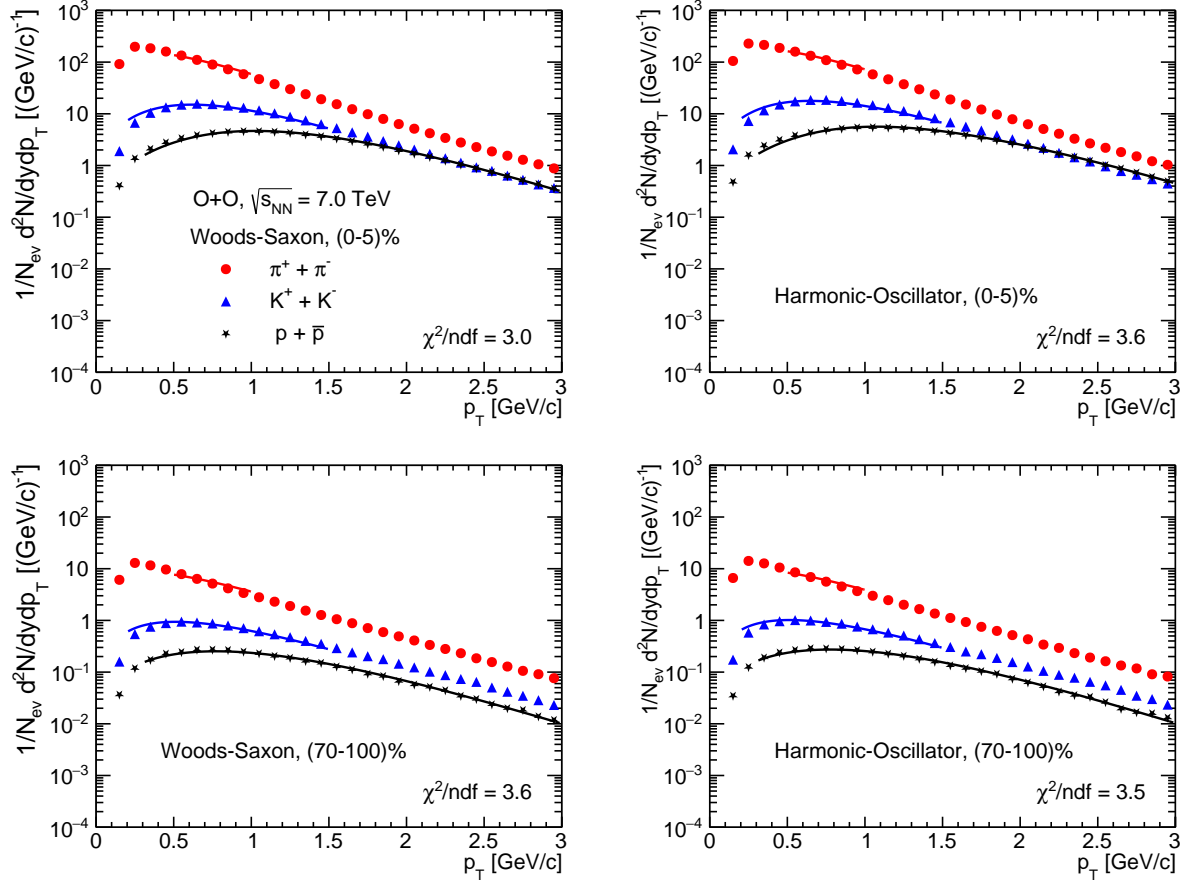


FIG. 7: (Color Online) Simultaneous fitting of identified particles' p_T -spectra with Boltzmann-Gibbs blastwave distribution in O+O collisions at $\sqrt{s_{NN}} = 7$ TeV for (0-5)% (top) and (70-100)% (bottom) centrality classes. The left (right) plots show the fitting with Woods-Saxon (Harmonic Oscillator) density profiles in the Oxygen nucleus.

fireball are assumed to move slower than the ones at the edges. The average of the transverse velocity is evaluated as [50],

$$\langle \beta_T \rangle = \frac{\int \beta_s \xi^n d\xi}{\int \xi d\xi} = \left(\frac{2}{2+n} \right) \beta_s. \quad (15)$$

For our calculation, we use n as a free parameter. Figure 8 shows the kinetic freeze-out temperature versus transverse radial flow from simultaneous fit of identified particles' p_T -spectra with Boltzmann-Gibbs blastwave distribution (Eq. 14) in O+O collisions at $\sqrt{s_{NN}} = 7$ TeV. The solid (open) markers represent the Woods-Saxon (harmonic oscillator) density profile. Within uncertainties, the correlation between kinetic freeze-out temperature (T_{kin}) and average transverse flow ($\langle \beta_T \rangle$) is similar for both density profiles. For the most central collisions (0-5% class), T_{kin} is the lowest and the transverse flow is highest. This behavior is expected as the most central collisions have the largest system size due to which the hadronic phase lasts longer, which makes the T_{kin} lowest. Also, due to the largest system size the radial flow is expected to be the highest. A similar behavior is seen

for Pb+Pb collisions at LHC energies [45].

TABLE III: Kinetic freeze-out temperature and transverse radial flow parameter obtained from Boltzmann-Gibbs blastwave fit using Eq. 14.

Centrality(%)	Woods-Saxon		harmonic oscillator	
	T_{kin} (GeV)	$\langle \beta_T \rangle$	T_{kin} (GeV)	$\langle \beta_T \rangle$
0-5	0.143 ± 0.013	0.65 ± 0.01	0.141 ± 0.016	0.67 ± 0.01
5-10	0.146 ± 0.015	0.64 ± 0.01	0.145 ± 0.007	0.66 ± 0.00
10-20	0.153 ± 0.019	0.63 ± 0.01	0.150 ± 0.231	0.65 ± 0.01
20-30	0.163 ± 0.014	0.61 ± 0.01	0.159 ± 0.015	0.63 ± 0.01
30-40	0.172 ± 0.018	0.59 ± 0.01	0.167 ± 0.016	0.61 ± 0.01
40-50	0.182 ± 0.017	0.57 ± 0.015	0.177 ± 0.022	0.58 ± 0.02
50-60	0.194 ± 0.013	0.54 ± 0.01	0.188 ± 0.013	0.56 ± 0.01
60-70	0.203 ± 0.015	0.52 ± 0.02	0.197 ± 0.014	0.53 ± 0.01
70-100	0.210 ± 0.015	0.50 ± 0.02	0.206 ± 0.008	0.50 ± 0.01

IV. PARTICLE RATIOS

Figure 9 shows p_T -differential kaon-to-pion and proton-to-pion ratios in O+O collisions at $\sqrt{s_{NN}} = 7$ TeV

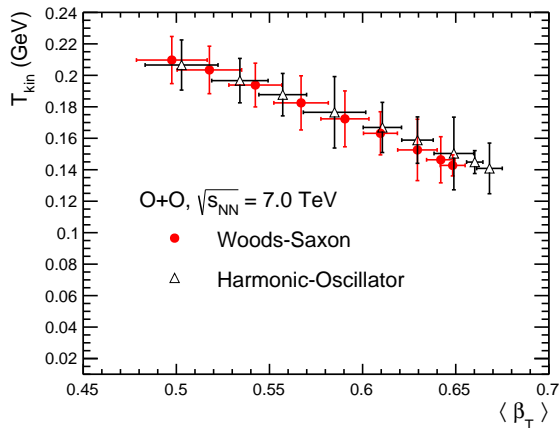


FIG. 8: (Color Online) Kinetic freeze-out temperature versus transverse radial flow from simultaneous fit of identified particles' p_T -spectra with Boltzmann-Gibbs blastwave distribution in O+O collisions at $\sqrt{s_{NN}} = 7$ TeV. The solid (open) markers represent the Woods-Saxon (harmonic oscillator) density profile.

for (0-5)% and (70-100)% centrality classes. Both the ratios to pions increase as a function of p_T . As the kaon-to-pion ratio is the measure of strangeness, we see enhancement of strangeness production as a function of p_T . This enhancement seems to be similar for both (0-5)% and (70-100)% centrality classes at low- p_T . However, the enhancement is higher for (0-5)% centrality class at intermediate- p_T . The proton-to-pion ratio, a ratio between lightest baryon to lightest meson, acts as a proxy to baryon to meson ratio. In general, the particle ratios do not show any dependence on the density profiles for (70-100)%. However, for (0-5)% centrality class, a rise in both kaon-to-pion and proton-to-pion ratios is seen at intermediate- p_T for harmonic oscillator density profile with respect to Woods-Saxon density profile, which becomes prominent at higher p_T .

V. ELLIPTIC FLOW

The initial spatial anisotropies of the overlap region in non-central heavy-ion collisions, gets converted to the momentum space azimuthal anisotropy of the final state particles due to the differential pressure gradients of the produced medium. The azimuthal anisotropy can be expressed as a Fourier series in the azimuthal angle, ϕ :

$$E \frac{d^3 N}{dp^3} = \frac{d^2 N}{2\pi p_T dp_T dy} \left(1 + 2 \sum_{n=1}^{\infty} v_n \cos[n(\phi - \psi_n)] \right), \quad (16)$$

where, v_n is the anisotropic flow of different order n , with $n = 2$ is elliptic flow. ψ_n is the n^{th} harmonic event plane angle [51]. To reduce the non-flow effects, a two-particle

correlation method [52, 53] can be adopted to estimate the elliptic flow. The correlation function between two particles is obtained in relative pseudorapidity ($\Delta\eta = \eta_a - \eta_b$) and relative azimuthal angle ($\Delta\phi = \phi_a - \phi_b$). Here, a and b denote two separate particles in a pair. In this study, we have taken charged particles in $|\eta| < 2.5$ and $p_T > 0.5$ GeV/c to be consistent with previous studies [52, 53].

The 1D correlation function is given as,

$$C(\Delta\phi) = \frac{dN_{\text{pairs}}}{d\Delta\phi} = A \times \frac{\int S(\Delta\eta, \Delta\phi) d\Delta\eta}{\int B(\Delta\eta, \Delta\phi) d\Delta\eta}, \quad (17)$$

where, the normalization constant (A) ensures that the number of pairs are the same between signal, $S(\Delta\eta, \Delta\phi)$ and background, $B(\Delta\eta, \Delta\phi)$. The $\Delta\eta$ interval is chosen carefully, as done in previous studies [52, 53], by excluding the jet peak region observed in the $C(\Delta\eta, \Delta\phi)$ distribution. The interval is taken to be $2.0 < |\Delta\eta| < 4.8$. This pseudorapidity cut removes the residual non-flow effects significantly in the estimation of elliptic flow. These non-flow correlations usually arise from jets and short range resonance decays, and they are not associated with the anisotropy in the early stage of the collisions. In the current study the non-flow effects are reduced significantly but they might be still non-zero. Thus, the quantitative interpretation of the results may be taken with caution.

The pair distribution can be expanded into a Fourier series:

$$\frac{dN_{\text{pairs}}}{d\Delta\phi} \propto \left[1 + 2 \sum_{n=1}^{\infty} v_{n,n}(p_T^a, p_T^b) \cos n\Delta\phi \right], \quad (18)$$

where, $v_{n,n}$ is the two particle flow coefficient. Now, Eq. 17 is given as:

$$C(\Delta\phi) \propto \left[1 + 2 \sum_{n=1}^{\infty} v_{n,n}(p_T^a, p_T^b) \cos n\Delta\phi \right]. \quad (19)$$

The definition of harmonics defined in Eq. 16 now enters in Eq. 18,

$$\frac{dN_{\text{pairs}}}{d\Delta\phi} \propto \left[1 + 2 \sum_{n=1}^{\infty} v_n(p_T^a) v_n(p_T^b) \cos n\Delta\phi \right]. \quad (20)$$

Through this definition, the event plane angle drops out in convolution. Thus, if the elliptic flow is driven by purely collective expansion then $v_{2,2}$ should be factorized into the product of two single-particle elliptic flow coefficients.

$$v_{2,2}(p_T^a, p_T^b) = v_2(p_T^a) v_2(p_T^b). \quad (21)$$

Using Eq. 21, we calculate the single particle elliptic flow coefficient as,

$$v_2(p_T^a) = v_{2,2}(p_T^a, p_T^b) / \sqrt{v_{2,2}(p_T^b, p_T^b)} \quad (22)$$

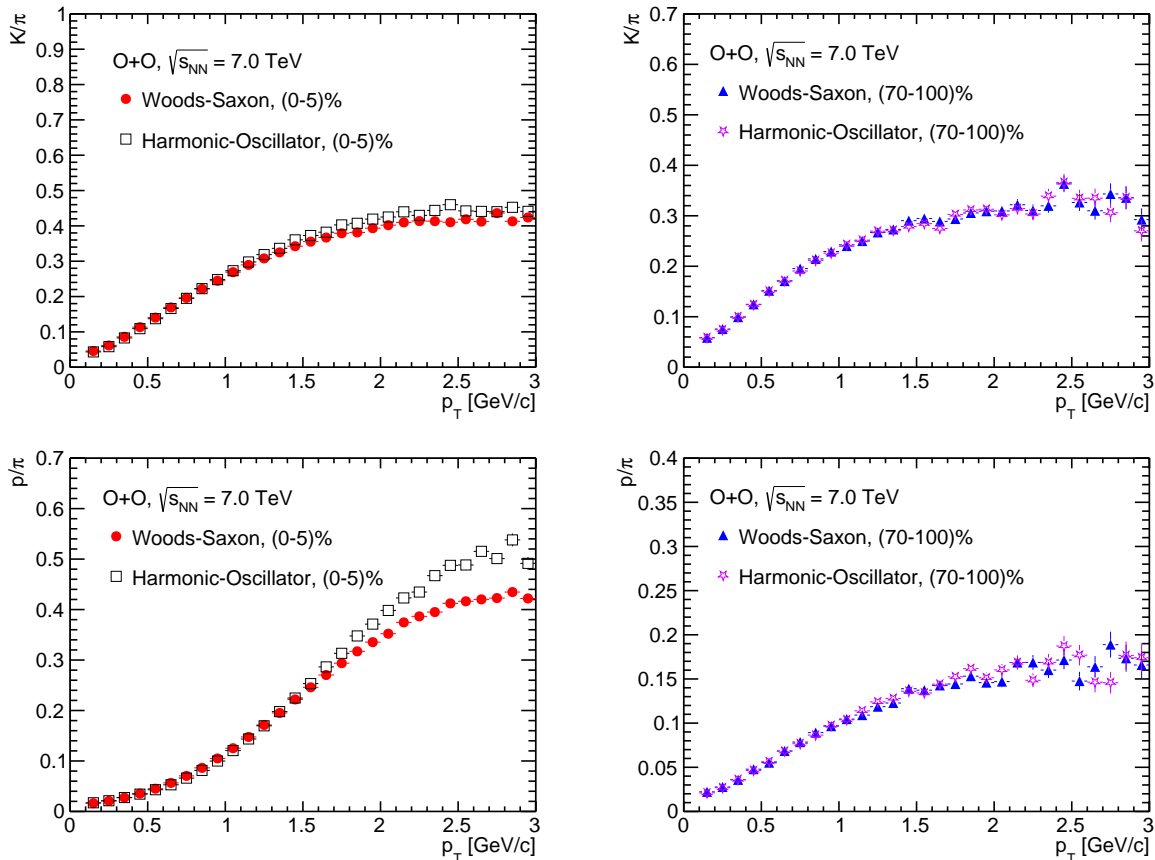


FIG. 9: (Color Online) p_T -differential kaon-to-pion (top) and proton-to-pion (bottom) ratio in O+O collisions at $\sqrt{s_{NN}} = 7$ TeV for (0-5)% (left) and (70-100)% (right) centrality classes. The solid (open) markers represent the Woods-Saxon (harmonic oscillator) density profile of oxygen nucleus.

We now proceed for the estimation of elliptic flow of charged particles as a function of transverse momentum for (20-30)% centrality class in O+O collisions at $\sqrt{s_{NN}} = 7$ TeV using AMPT for both the density profiles considered in this study. This is shown in Figure 10. v_2 is found to increase at low- p_T and saturates at intermediate- p_T . The qualitative trend of elliptic flow as a function of p_T in O+O collisions is found to be similar to that is observed by ALICE experiment in p+Pb collisions at $\sqrt{s_{NN}} = 5.02$ TeV [54]. Within uncertainties, v_2 is found to be similar for both the density profiles considered in this study. This indicates that, although there is a significant dependence of the initial energy density on the density profiles, the collectivity (both radial and elliptic flow) is less affected by the modification in the density profiles. However, to establish this behavior, a detailed study on centrality and transverse sphericity dependence of elliptic flow [52] and the impact of density profiles needs to be performed. It would be also interesting to compare the predictions of elliptic flow from AMPT with upcoming experimental results in O+O collisions.

VI. SUMMARY

In summary, we report the predictions for global properties in O + O collisions at $\sqrt{s_{NN}} = 7$ TeV using a multi-phase transport model (AMPT). We report the mid-rapidity charged particle multiplicity, transverse mass, Bjorken energy density, pseudorapidity distributions, speed of sound, p_T spectra and the kinetic freeze-out parameters as a function of collision centrality. The results are shown for both harmonic oscillator and Woods-Saxon nuclear density profiles incorporated for oxygen nucleus. With the change of the density profile from Woods-Saxon to harmonic oscillator, a modification of average charged-particle multiplicity is seen, which is also reflected in the initial energy density as one naively expects. However, other global properties show less dependence on the density profile considered in this work. In general, the initial energy density produced in all collision centralities in O+O collisions at $\sqrt{s_{NN}} = 7$ TeV stays higher than the lattice QCD predicted value for a deconfinement transition, making oxygen nucleus collision as a potential case of light-nuclei collisions at the LHC energies to create a state of QGP.

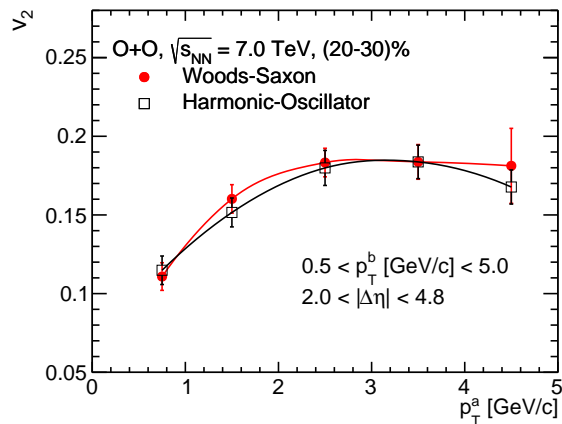


FIG. 10: (Color Online) Elliptic flow of charged particles as a function of transverse momentum in O+O collisions for (20-30)% centrality at $\sqrt{s_{NN}} = 7$ TeV. The solid (open) markers represent the Woods-Saxon (harmonic oscillator) density profile of oxygen nucleus.

In addition, a substantial radial flow and a comparable freeze-out temperature with that of Pb-Pb collisions is also observed from the present analysis. Although a significant dependence of the initial energy density on the density profiles is seen, the collectivity (both radial and elliptic flow) is less affected by the modification in the density profiles. It would be interesting to confront these results with the experimental observations, when available, to reveal about the density profile of oxygen nucleus from ultra-relativistic nuclear collisions.

Appendix

As the experimental data will be available for O+O collisions in future (LHC RUN3), we have compared the charged particle p_T -spectra from a collision system having closer system size to O+O collisions *i.e.*, minimum bias p+Pb collisions at $\sqrt{s_{NN}} = 5.02$ TeV with the predictions from AMPT. We have compared the AMPT predictions modifying the partonic scattering cross section, σ_{gg} to different values such as 3, 5 and 10 mb. The partonic scattering cross section is modified via the modification of lund string fragmentation parameters in AMPT. From this exercise, we found that fixing $\sigma_{gg} = 3$ mb, the AMPT predictions are closer to experimental data in p+Pb collisions at $\sqrt{s_{NN}} = 5.02$ TeV. Figure 11 shows the compari-

son of ALICE data with the predictions from AMPT with $\sigma_{gg} = 3$ mb for p-Pb collisions at $\sqrt{s_{NN}} = 5.02$ TeV. It is found that the spectral shape from AMPT matches with the experimental data at high- p_T while at intermediate- p_T , 10-30% difference is observed. One should also note here that, to exactly match with the experimental data, one can vary the tunes of the AMPT model, which is currently out of the scope of this manuscript.

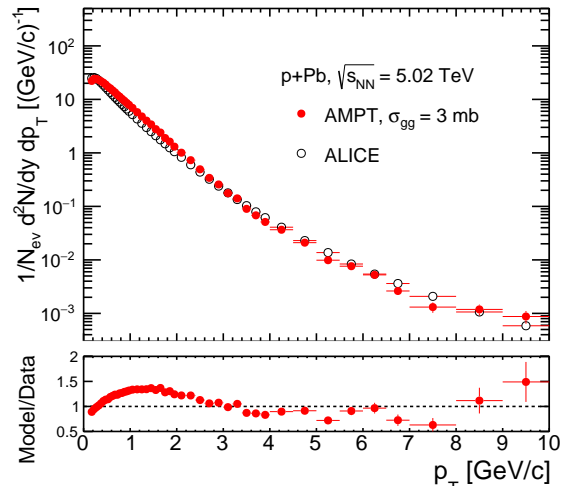


FIG. 11: (Color Online) Comparison of ALICE data with the predictions from AMPT with $\sigma_{gg} = 3$ mb for p-Pb collisions at $\sqrt{s_{NN}} = 5.02$ TeV.

Acknowledgements

DB acknowledges the financial supports from CSIR, Government of India. SP acknowledges the financial supports from UGC, Government of India. Raghunath Sahoo acknowledges the financial supports under the CERN Scientific Associateship, CERN, Geneva, Switzerland and the financial grants under DAE-BRNS Project No. 58/14/29/2019-BRNS of Government of India. ST acknowledges the supports under the INFN postdoctoral fellowship. A. N. M. thanks the Hungarian National Research, Development and Innovation Office (NKFIH) under the contract numbers OTKA K135515, K123815 and NKFIH 2019-2.1.11-TET-2019-00078, 2019-2.1.11-T ET-2019-00050 and the Wigner GPU Laboratory. The authors would like to acknowledge the usage of resources of the LHC grid computing facility at VECC, Kolkata and usage of resources of the LHC grid Tier-3 computing facility at IIT Indore.

- [1] J. Adam *et al.* [ALICE Collaboration], Nature Phys. **13**, 535 (2017).
 [2] V. Khachatryan *et al.* [CMS Collaboration], Phys. Lett. B **765**, 193 (2017).

- [3] J. Brewer, A. Mazeliauskas and W. van der Schee, arXiv:2103.01939 [hep-ph].
 [4] S. H. Lim, J. Carlson, C. Loizides, D. Lonardon, J. E. Lynn, J. L. Nagle, J. D. Orjuela Koop and J. Ouel-

- lette, Phys. Rev. C **99**, 044904 (2019).
- [5] M. Rybczyński and W. Broniowski, Phys. Rev. C **100** (2019), 064912.
- [6] S. Huang, Z. Chen, J. Jia and W. Li, Phys. Rev. C **101** (2020), 021901.
- [7] M. D. Sievert and J. Noronha-Hostler, Phys. Rev. C **100** (2019) 024904.
- [8] G. Röpke, P. Schuck, C. Xu, Z. Ren, M. Lyu, B. Zhou, Y. Funaki, H. Horiuchi, A. Tohsaki and T. Yamada, J. Low Temp. Phys. **189**, 383-409 (2017).
- [9] Y. A. Li, S. Zhang and Y. G. Ma, Phys. Rev. C **102**, 054907 (2020).
- [10] G. Gamow, Constitution of Atomic Nuclei and Radioactivity (Clarendon Press, Oxford, 1931).
- [11] J.A. Wheeler, Phys. Rev. **52**, 1083 (1937).
- [12] W. Broniowski and E. Ruiz Arriola, Phys. Rev. Lett. **112**, 112501 (2014).
- [13] P. Bozek, W. Broniowski, E. Ruiz Arriola and M. Rybczynski, Phys. Rev. C **90**, 064902 (2014).
- [14] P. Bozek and W. Broniowski, Phys. Lett. B **739**, 308 (2014).
- [15] Rohlf, James William, Modern Physics from α to Z0, Wiley, 1994.
- [16] Z. W. Lin, C. M. Ko, B. A. Li, B. Zhang and S. Pal, Phys. Rev. C **72**, 064901 (2005).
- [17] R. Kanungo *et al.* Phys. Rev. Lett. **102**, 152501 (2009).
- [18] L. Van Hove, Phys. Lett. B **118** (1982), 138.
- [19] J. D. Bjorken, Phys. Rev. D **27**, 140 (1983).
- [20] M. Kliemant, R. Sahoo, T. Schuster and R. Stock, Lect. Notes Phys. **785**, 23-103 (2010).
- [21] X. N. Wang and M. Gyulassy, Phys. Rev. D **44**, 3501 (1991).
- [22] B. Zhang, Comput. Phys. Commun. **109**, 93 (1998).
- [23] Z. w. Lin and C. M. Ko, Phys. Rev. C **65**, 034904 (2002).
- [24] Y. He and Z. W. Lin, Phys. Rev. C **96**, 014910 (2017).
- [25] B. Li, A. T. Sustich, B. Zhang and C. M. Ko, Int. J. Mod. Phys. E **10**, 267 (2001).
- [26] B. A. Li and C. M. Ko, Phys. Rev. C **52**, 2037 (1995).
- [27] R. J. Fries, B. Muller, C. Nonaka and S. A. Bass, Phys. Rev. Lett. **90**, 202303 (2003).
- [28] R. J. Fries, B. Muller, C. Nonaka and S. A. Bass, Phys. Rev. C **68**, 044902 (2003).
- [29] V. Greco, C. M. Ko and P. Levai, Phys. Rev. C **68**, 034904 (2003).
- [30] S. Tripathy, S. De, M. Younus and R. Sahoo, Phys. Rev. C **98**, 064904 (2018).
- [31] M. L. Miller, K. Reygers, S. J. Sanders and P. Steinberg, Ann. Rev. Nucl. Part. Sci. **57** (2007), 205.
- [32] C. Loizides, Phys. Rev. C **94**, 024914 (2016).
- [33] R. J. Glauber and G. Matthiae, Nucl. Phys. B **21**, 135 (1970).
- [34] C. Loizides, J. Kamin and D. d'Enterria, Phys. Rev. C **97**, 054910 (2018) Erratum: [Phys. Rev. C **99**, 019901 (2019)].
- [35] C. Loizides, *et al.*, <https://tglaubermc.hepforge.org/>
- [36] B. Alver, M. Baker, C. Loizides and P. Steinberg, arXiv:0805.4411 [nucl-ex].
- [37] C. Loizides, J. Nagle and P. Steinberg, SoftwareX **1-2** (2015), 13-18.
- [38] R. Sahoo, A. N. Mishra, N. K. Behera and B. K. Nandi, Adv. High Energy Phys. **2015**, 612390 (2015) [erratum: Adv. High Energy Phys. **2017**, 4517153 (2017)].
- [39] J. Adam *et al.* [ALICE Collaboration], Phys. Rev. C **94**, 034903 (2016).
- [40] B. I. Abelev *et al.* [STAR Collaboration], Phys. Rev. C **79**, 034909 (2009).
- [41] F. Karsch, Nucl. Phys. A **698** (2002), 199.
- [42] L. D. Landau, Izv. Akad. Nauk Ser. Fiz. **17**, 51 (1953).
- [43] E. Abbas *et al.* [ALICE Collaboration], Phys. Lett. B **726**, 610 (2013).
- [44] R. Sahoo, A. N. Mishra, N. K. Bahera and B. K. Nandi, Adv. High Energy Phys. **2015**, 612390 (2015).
- [45] S. Acharya *et al.* [ALICE Collaboration], Phys. Rev. C **101**, 044907 (2020).
- [46] E. Schnedermann, J. Sollfrank and U. W. Heinz, Phys. Rev. C **48**, 2462 (1993).
- [47] P. Huovinen, P. F. Kolb, U. W. Heinz, P. V. Ruuskanen and S. A. Voloshin, Phys. Lett. B **503**, 58 (2001).
- [48] P. Braun-Munzinger, J. Stachel, J. P. Wessels and N. Xu, Phys. Lett. B **344**, 43 (1995).
- [49] Z. Tang *et al.*, Chin. Phys. Lett. **30**, 031201 (2013).
- [50] K. Adcox *et al.* [PHENIX Collaboration], Phys. Rev. C **69**, 024904 (2004).
- [51] B. B. Abelev *et al.* [ALICE Collaboration], JHEP **1506**, 190 (2015).
- [52] N. Mallick, R. Sahoo, S. Tripathy and A. Ortiz, J. Phys. G **48**, 045104 (2021).
- [53] G. Aad *et al.* [ATLAS Collaboration], Phys. Rev. C **92**, 034903 (2015).
- [54] B. B. Abelev *et al.* [ALICE], Phys. Lett. B **726** (2013), 164.